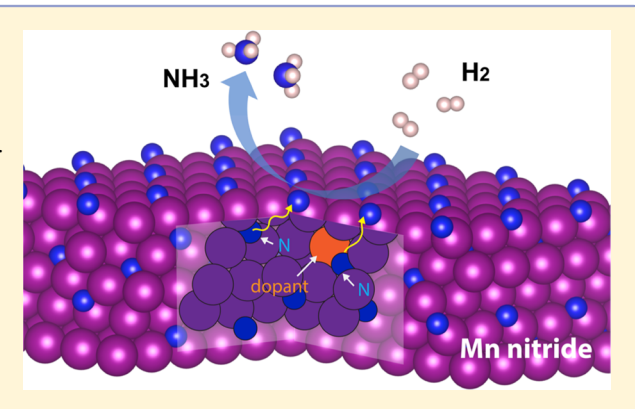


Fe and Ni Dopants Facilitating Ammonia Synthesis on Mn₄N and Mechanistic Insights from First-Principles Methods

Nannan Shan, †® Viktor Chikan, † Peter Pfromm, †, §® and Bin Liu†, *®

Supporting Information

ABSTRACT: Cyclic step-catalysis enables intermittent, atmospheric ammonia production, and can be integrated with sustainable and renewable energy sources. By employing metal (e.g., Mn) nitride, a nitrogen carrier, the rate-limiting N₂ activation step is bypassed. In this work, molecular-level pathways, describing the reduction of Mn₄N by dissociatively adsorbed hydrogen, were investigated using periodic density functional theory (DFT). The established mechanism confirmed that Fe and Ni doped in the nitride sublayer and top layer can disturb local electronic structures and be exploited to tune the ammonia production activity. The strength of N–M (M = Mn, Fe, Ni) and H–M bonds both determine the overall reduction thermochemistry. DFT-based modeling further showed that the low concentration of Fe or Ni in the Mn₄N sublayer facilitates N diffusion by lowering the diffusion energy barrier. Also,



these heteroatom dopant species, particularly Ni, decrease the reduction endergonicity, thanks to the strong hydrogen binding with the surface Ni dopant. The Brønsted–Evans–Polanyi relationship and linear scaling relationships have been developed to reveal ammonia evolution kinetic and energetic trends for a series of idealized Fe- and Ni-doped Mn_4N . Deviations from the linear scaling relationship have been observed for certain doped systems, indicating potentially more complex behaviors of metal nitrides and intriguing promises for greater ammonia synthesis materials design opportunities.

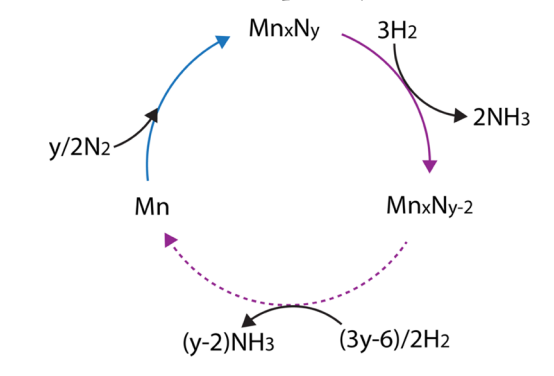
1. INTRODUCTION

Ammonia is the backbone of today's economy because of its use in agriculture that supports almost half the world's population. The Haber-Bosch process accounts for most of the ammonia production and consumes more than 1% of the global energy use.² Ammonia synthesis based on Haber-Bosch (at pressures up to 300 bar and temperatures up to 500 °C) is an energy-intensive process. In the last few decades, alternative solutions for ammonia synthesis using electrochemical^{3,4} or photocatalytic³ methods have been explored. Steinfeld and coworkers demonstrated a two-step solar-driven cyclic process for NH₃ synthesis, ⁶⁻⁸ in which aluminum oxide (Al₂O₃) was first reduced by N₂ to form aluminum nitride (AlN), which then reacts with water to produce NH₃. The reduced nitride can be recycled to participate in nitridation in the next cycle. While the reaction was conducted at ambient pressure, high temperature (1000–2000 °C) was required to reduce Al₂O₃.

Nitrides based on transition metals (e.g., Cr, Mn, and Fe) have been extensively examined experimentally in our previous work to generate NH $_3$ with H $_2$. It is concluded that manganese nitride was most promising because of its relatively favorable nitridation and reduction thermodynamics. The nitridation and reduction cycle involving manganese nitrides

is schematically shown in Scheme 1. The stoichiometry is included as the coefficient for each main species. Complete

Scheme 1. Nitridation (in Blue) and Reduction (in Purple) Cycle Describing Manganese Nitride (Mn_xN_y) and Ammonia (NH_3) Formation for the Step-Catalysis Process



Received: December 21, 2017
Revised: February 22, 2018
Published: February 26, 2018

[†]Department of Chemical Engineering and [‡]Department of Chemistry, Kansas State University, Manhattan, Kansas 66506, United States

[§]Voiland School of Chemical Engineering and Bioengineering, Washington State University, Pullman, Washington 99164, United States

reduction to pure Mn is represented by the dashed line. Moreover, the electronic structures of metal nitrides (such as Mn₂N and Sr₂N) were also explored using density functional theory (DFT) calculations in relation to metal nitridation and NH₃ production. 12 It has also been shown that nitrogen vacancy formation energy can be used as the descriptor to characterize nitride activity. To tune the activity of metal nitride, doping of Mn₂N with different metals, including Sc, Ti, V, Cr, Fe, Co, Ni, Cu, and Zn, have been evaluated, ¹³ indicating that the local electronic structure of Fe-doped Mn₂N destabilizes lattice nitrogen and facilitates the extraction of lattice nitrogen to produce NH3. More recently, group III-VII transition metal mononitrides have also been investigated for applications in the electrochemical synthesis of ammonia, which could expand the utilization of metal nitrides for NH3 production. 14-17

Although experiments indicated that manganese nitrides are promising nitrogen carriers for ammonia synthesis, ^{12,13} an avenue to evaluate their performance remains missing. This will further hinder the improvement of manganese nitrides by chemical doping or alloying. Mn₄N is an ideal starting-point material to tackle this issue. First, Mn₄N, along with Mn₆N_{2,58}, exists as one of manganese-based nitride phases involved in the cyclic transformation (see Scheme 1), as observed by Michalsky and Pfromm. ^{12,13} Second, Mn₄N has a simple face-centered cubic (FCC) crystal structure (Figure 1a). Both its crystallographic and magnetic properties have been well documented, compared with those of other phases especially Mn₆N_{2,58}. ^{18,19}

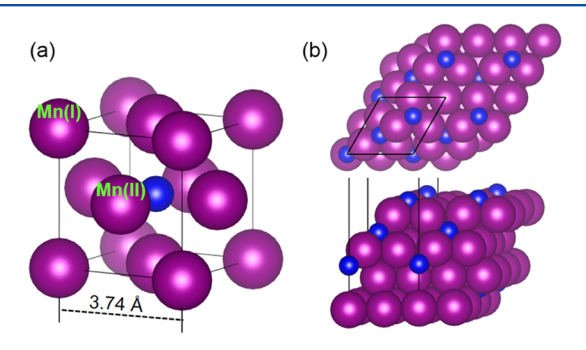


Figure 1. (a) Optimized bulk structure of the $\mathrm{Mn_4N}$ phase of manganese nitride; the two types of Mn atoms (I) and (II) are labeled. The lattice parameter of the cubic conventional cell is indicated. (b) Top (upper) and side (lower) views of N-terminated $\mathrm{Mn_4N}$ closepacked (111) surface. Mn and N are in magenta and blue, respectively. Black lines represent the periodic boundaries of the $p(1\times 1)$ unit cell of the $\mathrm{Mn_4N}(111)$ facet.

This study aims to provide detailed molecular mechanisms describing NH_3 production based on the Mn_4N phase of manganese nitride using DFT. Using the established reaction thermodynamics on the selected pure Mn_4N , suggestions have been made to tune the properties of Mn_4N with Fe and Ni dopants. The Brønsted–Evans–Polanyi (BEP) relationship and linear scaling relationship have been developed to reveal the reaction kinetic and energetic trends for a series of doped Mn_4N as guidance for novel materials design.

2. COMPUTATIONAL DETAILS

Spin-polarized DFT calculations were performed using the Vienna Ab initio Simulation Package. The electron–electron exchange—correlation energies were determined with the generalized gradient approximation Perdew—Burke—

Ernzerhof (GGA-PBE) functional.²² The projector-augmented wave (PAW) method²³ was used to describe electron—ion interactions.

The Mn₄N nitride phase has a FCC bulk structure, ^{18,24}as shown in Figure 1a. The bulk was optimized with a plane-wave cutoff energy of 420 eV and a $16 \times 16 \times 16$ Monkhorst–Pack k-point mesh. ²⁵ The lattice constant was converged to 3.74 Å, and the calculated magnetic moments are 3.31 $\mu_{\rm B}$ for Mn(I) and -0.90 $\mu_{\rm B}$ for Mn(II) (labeled in Figure 1a). These values are in good agreement with the corresponding experimental values, that is, 3.86 Å, 3.85 $\mu_{\rm B}$, and -0.9 $\mu_{\rm B}$. Potential self-interaction errors for Mn₄N were also considered by performing GGA + U calculations. The calculated results with various U values are shown in Table S1 and Figure S1 in the Supporting Information. However, these results indicate that standard DFT calculations (very small U) can adequately account for the structural and magnetic properties of Mn₄N.

A 4-layer, (1×1) Mn₄N(111) slab was employed for periodic DFT calculations. The bottom two layers were fixed to the optimized bulk value. The first Brillouin-zone of such a slab is sampled with a $4 \times 4 \times 1$ Monkhorst–Pack k-point mesh. The cutoff energy for the plane-wave basis set was set to be 380 eV for slab models. Self-consistent iterations were converged up to 1×10^{-6} eV, whereas the ionic steps were converged when the force on each atom is less than 0.02 eV/Å. Dipole corrections were included in all slab calculations.

Climbing image nudged elastic band²⁶ and dimer methods²⁷ were employed in search of the transition state (TS) of an elementary reaction step. A 5-layer slab with first 3 layers relaxing was used for TS searching. The reaction free energies (ΔG) were estimated based on $\Delta G = \Delta E + \Delta ZPE - T\Delta S$, where ΔE , ΔZPE , and $T\Delta S$ represent the electronic energy, zero point energy, and entropy terms, respectively. Vibrational frequencies were calculated using simple harmonic approximations. The entropy is estimated using the standard statistical mechanical approach, and computational details have been discussed in our previous work.^{28,29}

In a similar manner to the Mars—van Krevelen mechanism, ³⁰ the top-layer lattice N atom directly participates in the NH₃ production and will be consumed on the surface. The sublayer lattice N atom diffuses onto the surface enabling continuous ammonia synthesis. In this work, the reaction energy of N diffusion $(E_{\rm r \, vac})$, diffusion barrier of sublayer lattice N $(E_{\rm a \, vac})$, binding energy of N $(E_{\rm N \, vac})$, and adsorption energy of NH_x $(E_{\rm ads}, x=1, 2)$ are defined in eqs 1–4

$$E_{\rm r\,vac} = E_{\rm FS} - E_{\rm IS} \tag{1}$$

$$E_{\rm a \, vac} = E_{\rm TS} - E_{\rm IS} \tag{2}$$

$$E_{\text{N vac}} = E_{\text{N}}^* - E_{\text{vac}}^* - \frac{1}{2} E_{\text{N}_2(\text{gas})}$$
 (3)

$$E_{\rm ads} = E_{\rm NH_x}^* - E_{\rm vac}^* - E_{\rm NH_x(gas)}$$
 (4)

where the asterisk (*) suggests the open surface site. $E_{\rm IS}$, $E_{\rm TS}$, and $E_{\rm FS}$ are the energies of the initial state (IS), TS, and final state (FS) of N diffusion, respectively. Herein, the IS denotes the slab with N atom in the sublayer, whereas FS denotes the slab with a sublayer N vacancy. Configurations corresponding to these reaction states are shown in Figure 2a,b. $E_{\rm vac}^*$ is the energy of surface with a N vacancy on the surface, $E_{\rm N}^*$ (Figure 1b) and $E_{\rm NH_x}^*$ (x=1,2) represent total energies of the slabs

The Journal of Physical Chemistry C

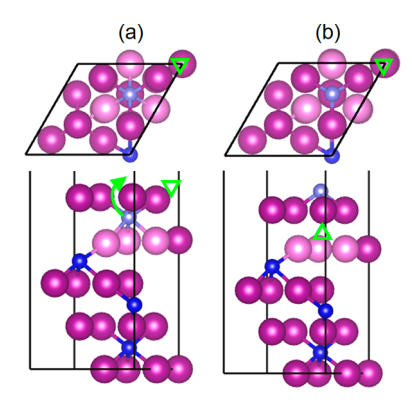


Figure 2. (a) IS and (b) FS of sublayer lattice N diffusion. Surface N vacancy site is shown with a downward green triangle, whereas sublayer N vacancy is indicated with an upward green triangle. Mn and N are in magenta and blue, respectively. The N and Mn atoms involved in diffusion are highlighted in light blue and purple. The green arrow shows the direction of N diffusion. Black lines represent the periodic boundaries of the $p(1 \times 1)$ unit cell.

with N and NH_x on the surface, and $E_{N_2(gas)}$ and $E_{NH_x(gas)}$ are the energies of N₂ and NH_x in the vacuum.

3. RESULTS AND DISCUSSION

3.1. Properties of Mn₄N. Asymmetric surface terminations can result from the cleavage of Mn₄N, as illustrated in Figure 1b, that is, N-terminated surface and Mn-terminated surface. The N-terminated surface was chosen as the reference so that the first reduction step begins with the surface N. The information for the Mn-terminated surface can be found in Figure S2 in Supporting Information.

The atomic H prefers to bind the 3-fold site on pure $Mn_4N(111)$, whereas NH^* , NH_2^* , and NH_3^* prefer to bind on the 3-fold, bridge, and top site, respectively. The reaction scheme describing the first NH_3 molecule formation can be expressed by steps (R1-R5), where "g", and "v" represent the gas phase and N vacancy site, respectively. In this study, the reduction sequence is assumed to start with gaseous H_2 dissociative adsorption forming H^* (shown in step R1). The adsorbed hydrogen atoms (H^*) then combine with N on $Mn_4N(111)$ stepwise to produce NH_3^* , as represented by R2-R4. NH_3^* desorbs leaving a vacancy $((v)_t)$ on the

 $Mn_4N(111)$ surface, as in step R5. Additional N will be provided via diffusions of $N_{(s)}$ on the sublayer in the Mn_4N sublayer lattice (R6).

$$\frac{1}{2}H_{2(g)} + * \to H^* \tag{R1}$$

$$H^* + N_{(t)} \rightarrow NH^* \tag{R2}$$

$$NH^* + H^* \rightarrow NH_2^* + *$$
 (R3)

$$NH_2^* + H^* \rightarrow NH_3^* + *$$
 (R4)

$$NH_3^* \to NH_{3(g)} + *(v)_t$$
 (R5)

$$N_{(s)} + *(v)_t \to N_{(t)} + *(v)_s$$
 (R6)

To control the reaction proceeding toward ammonia production, the experiment has to be carried out at elevated temperatures, sometimes up to $700\,^{\circ}\text{C}$ and 1 bar. ¹² In addition, the produced NH₃ needs to be extracted continuously, shifting the equilibrium toward NH₃ formation.

Here, the reaction free energies, estimated at 700 °C and 1 bar for the reduction of stoichiometric Mn_4N at its close-packed (111) facet, are shown in Figure 3. This reaction condition was determined according to the experimental work reported in ref 12. Clean surface (Figure 1b) and gas phase H_2 were used as the zero energy reference state (note: nitrogen is supplied by Mn_4N). Optimized geometries of the reaction intermediates at their preferred sites are illustrated in the top panels of Figure 3. The process to produce two NH_3 is expressed according to the stoichiometry of $3H_{2(g)} + 2N_{(lat)} \rightarrow 2NH_{3(g)}$, utilizing one top-layer lattice N ($N_{(t)}$) and one sublayer lattice N ($N_{(s)}$).

On $\mathrm{Mn_4N(111)}$, hydrogen dissociative adsorption (R1) is endergonic (0.26 eV/H atom). The formation of NH* (R2) is an exergonic step (-0.33 eV) resulting in one N-H bond formation. Subsequent NH₂* and NH₃* formations are also endergonic (at respective 0.83 and 0.66 eV). The release of NH₃ is an exergonic step (-0.68 eV), mainly because of the gain of entropy. Once the original N_(t) is consumed, the lattice N in the sublayer is expected diffuse onto the surface, overcoming an energy barrier of 1.12 eV. Hence, as shown in Figure 3, the reduction sequences between each NH₃

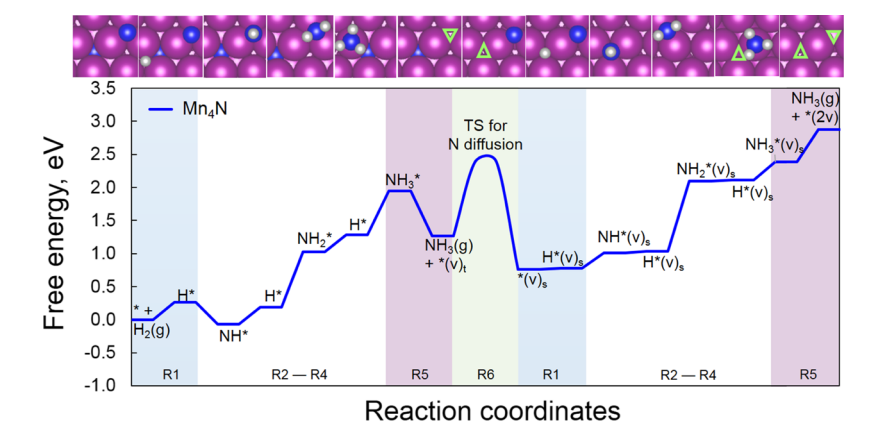


Figure 3. Free energy diagram for $Mn_4N(111)$ surface reduction by H_2 (two NH_3 molecules produced based on the stoichiometry of $3H_{2(g)} + 2N_{(lat)} \rightarrow 2NH_{3(g)}$) at 700 °C and 1 bar. Optimized structures corresponding to each intermediate elementary step are also shown. Surface N vacancy sites are shown with a downward green triangle, whereas sublayer N vacancy sites are indicated with an upward green triangle. The vacancy sites are not shown for N*, NH*, and NH*, as they are underneath the adsorbates and hidden. Mn, N, and H are in magenta, blue, and gray, respectively.

production being considered are connected by one step of lattice N diffusion from the sublayer onto the top layer (R6). This nitrogen transport step is crucial as it ensures the supply of N species for continuous NH₃ formation. With the formation of a new $N_{(t)}$ species, a sublayer nitrogen vacancy, $(v)_s$, is formed at the same time. In the second NH3 formation sequence, hydrogen dissociative adsorption is slightly endergonic (0.02 eV). The corresponding free energies for NH*, NH₂, and NH₃ formations are 0.23, 1.06, and 0.27 eV, respectively. It can be noted that the formation of NH* becomes more endergonic than the same step in the first sequence. It is also interesting to note that the formation of second NH₃ becomes less endergonic (0.27 vs 0.66 eV). The observed variations in the reaction free energies can be considered to be due to the influence of the sublayer nitrogen vacancy, (v)_s. Overall, the formation of the second NH₃ is still an endergonic process.

According to the proposed mechanism (R1–R6), two potential performance-limiting factors influencing the NH₃ formation activity have been identified: (1) binding energies of H/NH₂/NH₃ on Mn₄N surfaces and (2) sublayer lattice N diffusion barrier ($E_{\rm a \ vac}$). The first factor can influence the overall NH₃ formation free energy ($\Delta G_{\rm NH_3^*}$), whereas the second factor determines the kinetics of nitrogen-supply to the surface. With the pure Mn₄N model, lower both $\Delta G_{\rm NH_3^*}$ and $E_{\rm a \ vac}$ will improve the manganese nitride performance in favor of NH₃ formation on the thermodynamic and kinetic aspects.

3.2. Behaviors of Mn₄N Doped with Fe and Ni. Doped manganese nitride showed the enhanced activity for ammonia synthesis experimentally. Given the weaker bonding strength with nitrogen in the nitride phase, Fe and Ni have been selected as candidates to tune the electronic properties of manganese nitride to increase the yield of ammonia. The top and side views of the doped models are depicted in Figure 4a,b. In the

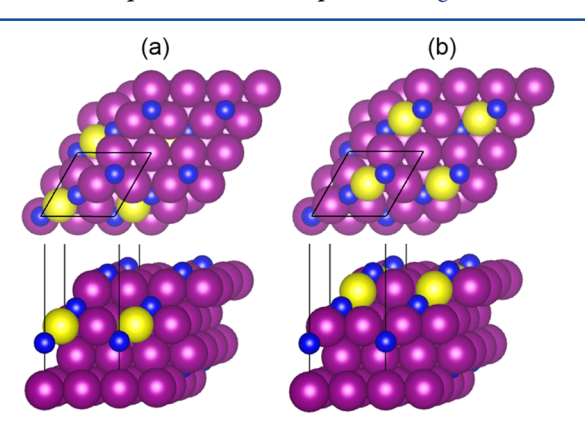


Figure 4. Top and side views of (a) sublayer and (b) top-layer doped $\mathrm{Mn_4N}(111)$ surface models with the N-termination. Mn, N, and the dopant atom are in magenta, blue, and yellow, respectively. Black lines represent the periodic boundaries of the $p(1 \times 1)$ unit cell.

structure with a single Fe atom dopant, the Mn atom is substituted in either the sublayer or the top layer, denoted by $Fe_s@Mn_4N$ and $Fe_t@Mn_4N$, respectively. Similarly, Ni-doped Mn_4N was denoted by $Ni_s@Mn_4N$ and $Ni_t@Mn_4N$. Bader charge analyses for pure and doped Mn_4N are illustrated in Figure S3. Free energies diagrams (at 700 °C and 1 bar) for the reductions of the Fe-doped Mn_4N nitrides ($Fe_s@Mn_4N$ and $Fe_t@Mn_4N$) are shown in Figure 5, where the free energies for

pure $\mathrm{Mn_4N}$ system (blue dashed lines) are included as a reference system.

On Fe_s@Mn₄N, free energies for elementary steps of R1–R5 in the first NH₃ formation sequence show negligible variations from those on pure Mn₄N (i.e., green vs blue dashed paths). Optimized structures on preferred sites of H*, NH*, NH₂*, and NH₃* resemble closely to those obtained on pure Mn₄N(111). This behavior indicates that with Fe in the sublayer, the impact on the interactions between H* and NH_x* (x = 1, 2, 3) intermediates with top-layer Mn atoms, in terms of Mn–H and Mn–N bond strength, is negligible.

Nevertheless, the energy barrier ($E_{\rm a\ vac}$) for step R6, involving the doped sublayer Fe atom, is lowered from 1.12 eV (Figure 6a) to 0.56 eV (Figure 6b), suggesting that the sublayer Fe facilitates the diffusion of $N_{(s)}$ onto the surface. For $N_{(s)}$ to move onto the top layer, this nitrogen atom is required to break the bond with the neighboring atoms (Mn or dopant) in the second layer. Because the Fe–N bond is weaker than the Mn–N bond, 13 the required energy that contributes to the overall energy barrier is expected to be lower. Moreover, at the TS and its proximity (in Figure 6b), the surface Mn atom is noticeably distorted from its normal lattice position; thus, the mechanical hindrance for the diffusion of the $N_{(s)}$ species can also be minimized.

Once a new $N_{(t)}$ becomes available, the second reduction sequence continues by following steps R1-R5. According to Figure 5 (green), the dissociative adsorption of hydrogen (R1) becomes exergonic (-0.22 eV). The free energy for this step is over 0.5 eV lower than that in the first reduction cycle (0.30 eV). Although NH* and NH2 formations (R2 and R3) are still endergonic (0.15 and 1.19 eV), the overall free energies for the second reduction circle becomes much less endergonic than on pure Mn₄N because of the more favorable H binding. NH₃* formation on Fe_s@Mn₄N is more endergonic (1.23 eV) than that on pure Mn₄N (0.27 eV). Unlike Mn₄N, the second NH₃ release step (R5) is exergonic by -0.66 eV (vs 0.49 eV on pure Mn₄N surface). This, again, can be attributed to Fe doping, as the Fe-N bond is weaker than the Mn-N bond, and the reduction of iron nitrides tends to be more thermodynamically favorable.1

On Fe_t@Mn₄N (the red path in Figure 5), a surface Mn atom is substituted by one Fe atom. The hydrogen dissociative adsorption (R1) becomes slightly less favorable than on pure Mn₄N (0.33 vs 0.26 eV), where the dissociated H atom binds at the 3-fold site consisting of the surface Fe dopant. However, the formations of NH* and NH $_2^*$ (R2 and R3) become slightly more favorable with free energies of -0.38 and 0.76 eV compared with corresponding steps on pure Mn₄N (-0.33 and 0.83 eV), respectively. As shown in bottom panels of Figure 5, NH* and NH $_2^*$ bind in the proximity to the surface Fe. Similarly, the NH $_3^*$ formation (R4) becomes thermodynamically favored as free energy is lowered from 0.66 eV (on pure Mn₄N) to 0.40 eV.

The energy barrier for $N_{(s)}$ diffusion $(E_{a \text{ vac}})$ is 1.09 eV in $\text{Fe}_t @ Mn_4 N$, which is only slightly lower than that in pure $Mn_4 N$ (1.12 eV). As shown in Figure 6c, $N_{(s)}$ needs to break the Mn–N bond with the Mn atom in the sublayer to diffuse onto the surface, whereas the Fe–N bond is retained. In addition, no dislocation of surface atoms near the TS is observed.

Although the surface Fe dopant does not enhance the lattice N diffusion as Fe_s@Mn₄N, the free energies for the second reduction cycle become thermodynamically favored than those

The Journal of Physical Chemistry C

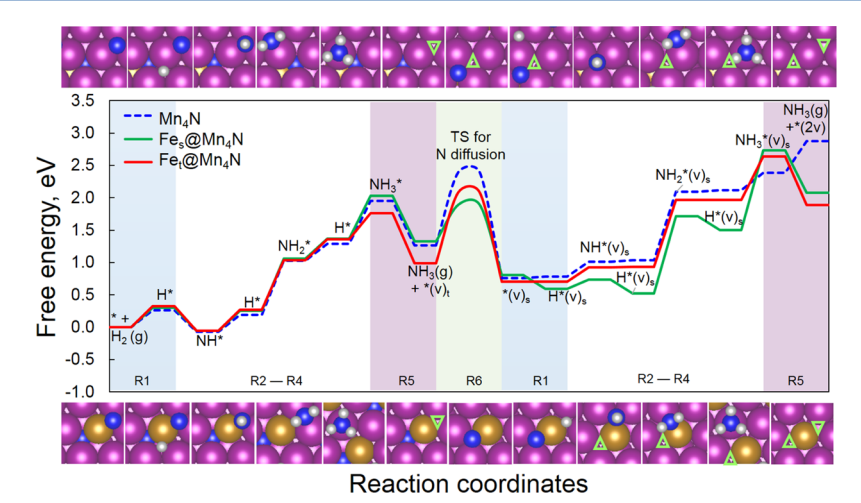


Figure 5. Free energy diagrams for the reduction of pure Mn_4N (blue dashed lines), $Fe_s@Mn_4N$ (green), and $Fe_t@Mn_4N$ (red) at 700 °C and 1 bar. Similarly, optimized structures for each intermediate step on the close-packed surface of $Fe_s@Mn_4N$ (top panels) and $Fe_t@Mn_4N$ (bottom panels) are shown. The surface N vacancy is represented with a downward green triangle, whereas the sublayer N vacancy is represented with an upward green triangle. Mn, Fe, N, and H are in magenta, gold, blue, and gray, respectively.

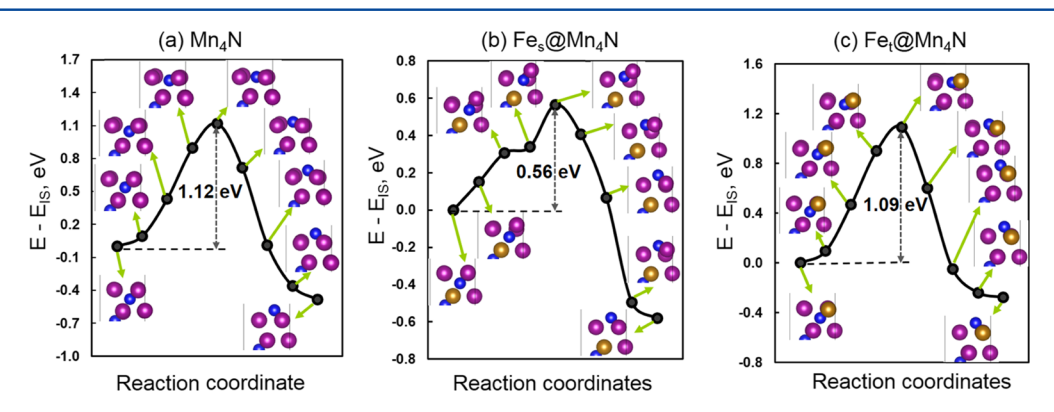


Figure 6. Potential energy surfaces for diffusions of $N_{(s)}$ from the sublayer to the surface on (a) pure Mn_4N , (b) $Fe_s@Mn_4N$, and (c) $Fe_t@Mn_4N$. The total energy of the IS (E_{IS}) is chosen as the energy reference. The snapshot image corresponding to each intermediate state is shown. Mn, Fe, Ni, and N are in magenta, gold, green, and blue, respectively.

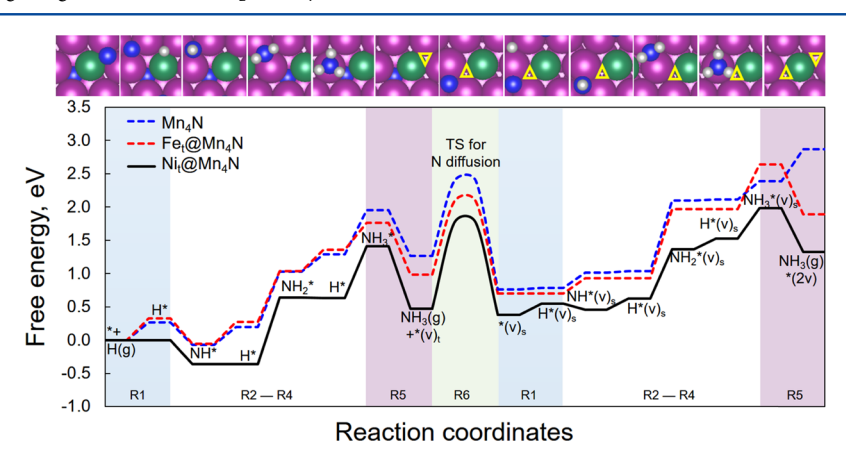


Figure 7. Free energy diagrams for the reduction of pure Mn_4N (blue dashed lines), $Fe_t@Mn_4N$ (red dashed lines), and $Ni_t@Mn_4N$ (black) at 700 °C and 1 bar. Similarly, the optimized structures for intermediate steps on the close-packed surface of $Ni_t@Mn_4N$ (top panels) are shown. Surface N vacancy is represented with a downward yellow triangle, whereas the sublayer N vacancy is represented with an upward yellow triangle. Mn, Ni, N, and H are in magenta, green, blue, and gray, respectively.

of pure Mn_4N , especially for the release the second NH_3 (-0.75 vs 0.49 eV on pure Mn_4N). This means that Fe doping can indeed reduce the endergonicity of ammonia formation regardless of the doping location. Furthermore, it can be

expected that Mn_4N modified with elements forming weaker bonds with nitrogen can achieve the similar effects.

Although Fe doping provides the means to lower the overall NH_3 formation endergonicity, modification of Mn_4N by tuning the hydrogen dissociative adsorption step (R1) would, in

principle, further enhance ammonia formation by shifting the overall reaction toward the thermodynamically favored direction. In this case, Ni (with stronger Ni–H bonding) has been selected to tune Mn_4N via similar substitutions of the sublayer and the top-layer Mn atoms.

Free energies for the hydrogen reduction of Mn₄N doped with Ni at its top-layer (Ni_t@Mn₄N) are shown in Figure 7 (black). Pure Mn₄N (blue dashed lines) and Fe₄@Mn₄N (red dashed lines) were included as references. Comparisons of free energies between pure Mn₄N, sublayer Ni doping (Ni₆@ Mn₄N), and Ni₄@Mn₄N are shown in Figure S4 in Supporting Information. On Ni_t@Mn₄N, hydrogen dissociative adsorption (R1) is almost thermal neutral (-0.001 eV at 700 °C and 1 bar), where the dissociated H* adsorbs at the 3-fold site next to the Ni dopant (the 2nd top panel of Figure 7), reflecting the direct involvement of doped top-layer Ni atom. The R1 step has become approximately 0.3 eV lower in free energy than that of both Mn₄N and Fe_t@Mn₄N. The adsorption patterns of NH_r^* (x = 1-3) resemble those on both Mn_4N and Fe_t Mn₄N. Therefore, the trends for R2-R4 steps are similar as expected. The stronger Ni-H bonding substantially reduces the overall free energies for the first NH3 production. In the second reduction cycle, although the free energy of the R1 step shifts upward to 0.16 eV (as H binding becomes weaker) when compared with that of Mn₄N (0.02 eV), the overall free energy for the second NH3 formation remains more favorable than Mn₄N. As shown in Figure 7, the overall free energy (forming two molecules of NH₃) is 1.55 eV lower than that on Mn₄N and 0.57 eV lower than that on Fe_t@Mn₄N.

Regarding N diffusion, the same principle can be applied to understand $N_{(s)}$ diffusion energy barrier of Step R6 for Nidoped Mn_4N . As shown in Figure 8a, compared with pure

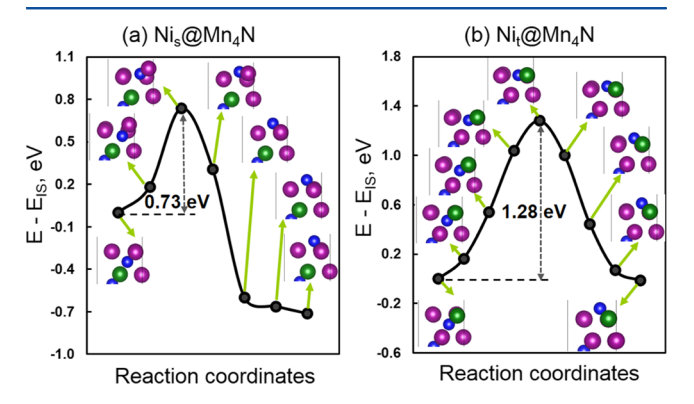


Figure 8. Potential energy surfaces for diffusions of $N_{(s)}$ from the sublayer to surface on (a) $Ni_s@Mn_4N$ and (b) $Ni_t@Mn_4N$. The total energy of the IS (E_{IS}) is chosen as the energy reference. The snapshot image corresponding to each intermediate state is shown. Magenta, green, and blue colors represent Mn, Ni, and N, respectively.

 $\rm Mn_4N$, $E_{\rm a\ vac}$ is lowered from 1.12 to 0.73 eV on $\rm Ni_s@Mn_4N$, suggesting that like the Fe dopant in the $\rm Mn_4N$ sublayer, the sublayer Ni also facilitates $\rm N_{(s)}$ diffusion onto the top layer because of the weaker Ni–N bond than the Mn–N bond. Similarly, the surface Mn atom is found distorted from its normal lattice position (Figure 8a). On $\rm Ni_t@Mn_4N$, the $E_{\rm a\ vac}$ has increased to 1.28 eV from 1.12 eV. This is due to the fact that $\rm N_{(s)}$ needs to break the Mn–N bond that is stronger than the Ni–N bond in $\rm Ni_t@Mn_4N$.

In order to reveal potential trends and predict the behaviors of Mn_4N doped with Fe and Ni, a correlation between the

reaction energy of N diffusion $(E_{\rm r\,vac})$ and diffusion barrier $(E_{\rm a\,vac})$ can be represented within the formulation of the well-established BEP relationship, as shown in Figure 9a. The slope and intersection are 0.96 (dimensionless) and 1.34 eV, respectively. As aforementioned, by referencing to pure Mn₄N, lower N diffusion barriers can be expected if weaker bonds (e.g., Fe–N and Ni–N bonds) need to be broken during N diffusion. On the other hand, the Cr–N bond is much stronger than the Mn–N bond. As a result, a decreased N diffusion barrier was observed for $Cr_t@Mn_4N$ instead because the weaker Mn–N bond broke for the sublayer N to diffuse onto the surface. In addition, for $Cr_s@Mn_4N$, the stronger Cr–N bond has to break, thus resulting in high barrier.

Finally, linear scaling relationships between $E_{\text{N vac}}$ and E_{ads} for NH_x^* (x = 1, 2) on pure and various doped Mn_4N , calculated according to eqs 3 and 4, are shown in Figure 9b, where data from calculations on Fe_s@Mn₄N, Fe_t@Mn₄N, Ni_s@Mn₄N, and Ni_t@Mn₄N were employed. Moreover, to test the limits of these scaling relationships for doped Mn₄N systems, sub- and top-monolayer configurations composed of Fe, denoted as Fe_{sm}@Mn₄N and Fe_{tm}@Mn₄N, were included (see Figure S5 in Supporting Information). With Mn₄N as the host material, linear correlations indeed exist between the two sets of quantities associated with NH* and NH2. Slopes of the two linear scaling relationships from fitting are 0.52 and 0.39 for NH* and NH₂* (standard error being 0.07 eV), respectively, close to the previous finding.³¹ The slopes are also within reasonable agreement with theoretical slopes, that is, 0.67 and 0.33 for respective NH* and NH₂* based on $(n_{\text{max}} - x)/n_{\text{max}}$ where $n_{\text{max}} = 3$, established on transition metals.

However, unlike metals, chemical properties of nitrides (e.g., Mn_4N) will be susceptible to the existence of sublayer N vacancies, which are likely to complicate the trends for reaction energetics prediction. As shown in Figure S6 in the Supporting Information, linear scaling relationships on Mn_4N and Fe- and Ni-doped Mn_4N surfaces with one sublayer N vacancy show varying slopes and intercepts for NH_x (x=1,2). It is also interesting to note large deviations on $Ni_{sm}@Mn_4N$ and $Ni_{tm}@Mn_4N$ surfaces in Figure 9b (denoted with red symbols). This observation suggests that the linear scaling relationships can be broken for certain configurations, possibly for mixed alloy nitrides as well. Nevertheless, these exceptions could offer exciting opportunities to design new nitride materials for NH_3 production.

4. CONCLUSIONS

Step-catalysis with metal nitride as the nitrogen source is regarded as a sustainable avenue for ammonia production. Although manganese nitrides are regarded to be promising for ammonia synthesis, theoretical insights become even more necessary by providing the mechanism to guide the discovery and design of novel materials. In this work, Mn₄N has been studied with DFT calculations to improve NH₃ production. The mechanism, describing hydrogen dissociative adsorption, lattice N diffusion, and ammonia formation, has been shown in detail. Thermodynamic analysis showed that the binding of atomic H and lattice N diffusion energy barrier are critical for the performance of manganese nitrides. Fe- and Ni-doped in the sublayer of Mn₄N are revealed to facilitate N diffusion, whereas both the sublayer and top-layer Ni dopants are able to lower the overall endergonicity due to favorable H adsorption. Furthermore, the energetic and kinetic behaviors of various configurations of doped Mn₄N have been summarized in terms

The Journal of Physical Chemistry C

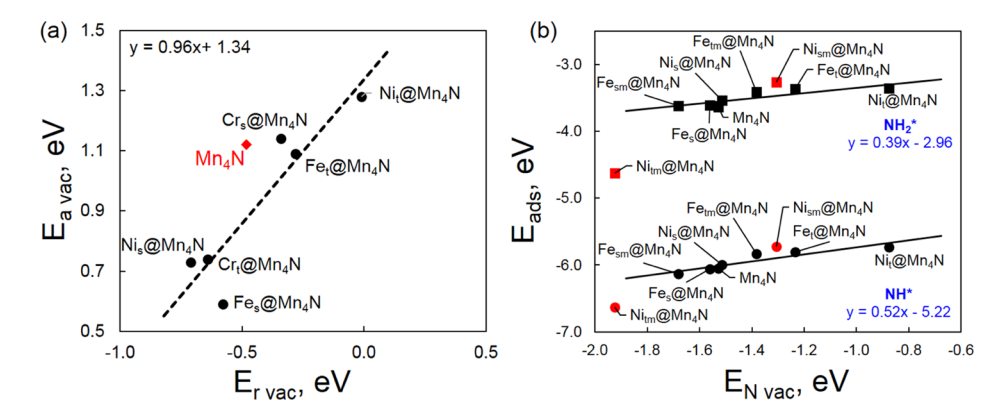


Figure 9. (a) BEP relationship for N diffusion, where $E_{r \text{ vac}}$ is the reaction energy of N diffusion based on eq 1. Pure Mn₄N is shown in red diamond. (b) Scaling relationships (black) between N binding energies ($E_{N \text{ vac}}$) and adsorption energies of NH* (circle) and NH₂* (square). Ni_{sm}@Mn₄N and Ni_{tm}@Mn₄N are included as outliners (in red) that do not follow the linear scaling.

of the BEP and linear scaling relationships, setting up the groundwork for future studies.

ASSOCIATED CONTENT

S Supporting Information

The Supporting Information is available free of charge on the ACS Publications website at DOI: 10.1021/acs.jpcc.7b12569.

Calculated lattice constant and magnetic momentum of $\rm Mn_4N$ with various U values; free energy diagram for $\rm NH_3$ production on pure and sublayer Fe-doped Mnterminated $\rm Mn_4N$ at 700 °C and 1 bar; bader charge analyses for pure and doped $\rm Mn_4N$; free energy diagrams for $\rm NH_3$ production on pure and Ni-doped N-terminated $\rm Mn_4N$ at 700 °C and 1 bar; configurations of sub- and top-monolayer doped N-terminated $\rm Mn_4N$ (111) surface; and scaling relationships between $E_{\rm N}$ vac and $E_{\rm ads}$ of $\rm NH^*$ and $\rm NH_2^*$ on the surfaces with a N vacancy in the sublayer (PDF)

AUTHOR INFORMATION

Corresponding Author

*E-mail: binliu@ksu.edu.

ORCID

Nannan Shan: 0000-0002-7700-6246 Peter Pfromm: 0000-0003-4869-9503 Bin Liu: 0000-0001-7890-7612

Notes

The authors declare no competing financial interest.

ACKNOWLEDGMENTS

The authors thank the financial support provided by the U.S. Department of Energy, Office of Science, Office of DOE EPSCOR, under Award Number(s) DOE EPSCOR DE-FOA-0001572. The authors are also grateful for the supercomputing resources and services from the Centre for Nanoscale Materials (CNM) supported by the Office of Science of the US Department of Energy under the contract no. DE-AC02-06CH11357, the Beocat Research Cluster at Kansas State University, which is funded in part by NSF grants CNS-1006860, and the National Energy Research Scientific Computing Centre (NERSC) under the contract no. DEAC02-05CH11231.

REFERENCES

- (1) Smil, V. Detonator of the Population Explosion. *Nature* **1999**, 400, 415.
- (2) Erisman, J. W.; Sutton, M. A.; Galloway, J.; Klimont, Z.; Winiwarter, W. How A Century of Ammonia Synthesis Changed the World. *Nat. Geosci.* **2008**, *1*, 636–639.
- (3) Amar, I. A.; Lan, R.; Petit, C. T. G.; Tao, S. Solid-state Electrochemical Synthesis of Ammonia: A Review. *J. Solid State Electrochem.* **2011**, *15*, 1845–1860.
- (4) Licht, S.; Cui, B. C.; Wang, B.; Li, F.-F.; Lau, J.; Liu, S. Ammonia Synthesis by N₂ and Steam Electrolysis in Molten Hydroxide Suspensions of Nanoscale Fe₂O₃. *Science* **2014**, *345*, 637–640.
- (5) Schrauzer, G. N.; Guth, T. D. Photocatalytic Reactions. 1. Photolysis of Water and Photoreduction of Nitrogen on Titanium Dioxide. *J. Am. Chem. Soc.* **1977**, *99*, 7189–7193.
- (6) Gálvez, M. E.; Halmann, M.; Steinfeld, A. Ammonia Production via A Two-step Al₂O₃/AlN Thermochemical Cycle. 1. Thermodynamic, Environmental, and Economic Analyses. *Ind. Eng. Chem. Res.* **2007**, *46*, 2042–2046.
- (7) Gálvez, M. E.; Frei, A.; Halmann, M.; Steinfeld, A. Ammonia Production via a Two-Step Al₂O₃/AlN Thermochemical Cycle. 2. Kinetic Analysis. *Ind. Eng. Chem. Res.* **2007**, *46*, 2047–2053.
- (8) Gálvez, M. E.; Hischier, I.; Frei, A.; Steinfeld, A. Ammonia Production via a Two-Step Al₂O₃/AlN Thermochemical Cycle. 3. Influence of the Carbon Reducing Agent and Cyclability. *Ind. Eng. Chem. Res.* **2008**, 47, 2231–2237.
- (9) Michalsky, R.; Pfromm, P. H. Thermodynamics of Metal Reactants for Ammonia Synthesis from Steam, Nitrogen and Biomass at Atmospheric Pressure. *AIChE J.* **2012**, *58*, 3203–3213.
- (10) Michalsky, R.; Parman, B. J.; Amanor-Boadu, V.; Pfromm, P. H. Solar Thermochemical Production of Ammonia from Water, Air and Sunlight: Thermodynamic and Economic Analyses. *Energy* **2012**, *42*, 251–260.
- (11) Michalsky, R.; Pfromm, P. H. An Ionicity Rationale to Design Solid Phase Metal Nitride Reactants for Solar Ammonia Production. *J. Phys. Chem. C* **2012**, *116*, 23243–23251.
- (12) Michalsky, R.; Avram, A. M.; Peterson, B. A.; Pfromm, P. H.; Peterson, A. A. Chemical Looping of Metal Nitride Catalysts: Low-pressure Ammonia Synthesis for Energy Storage. *Chem. Sci.* **2015**, *6*, 3965–3974.
- (13) Michalsky, R.; Pfromm, P. H.; Steinfeld, A. Rational Design of Metal Nitride Redox Materials for Solar-driven Ammonia Synthesis. *Interface Focus* **2015**, *5*, 20140084.
- (14) Abghoui, Y.; Garden, A. L.; Howalt, J. G.; Vegge, T.; Skúlason, E. Electroreduction of N_2 to Ammonia at Ambient Conditions on Mononitrides of Zr, Nb, Cr, and V: A DFT Guide for Experiments. ACS Catal. 2016, 6, 635–646.
- (15) Abghoui, Y.; Skúlason, E. Computational Predictions of Catalytic Activity of Zincblende (110) Surfaces of Metal Nitrides for

- Electrochemical Ammonia Synthesis. J. Phys. Chem. C 2017, 121, 6141–6151.
- (16) Abghoui, Y.; Skúlason, E. Onset Potentials for Different Reaction Mechanisms of Nitrogen Activation to Ammonia on Transition Metal Nitride Electro-catalysts. *Catal. Today* **2017**, 286, 69–77.
- (17) Abghoui, Y.; Skúlason, E. Electrochemical Synthesis of Ammonia via Mars-van Krevelen Mechanism on the (111) Facets of Group III–VII Transition Metal Mononitrides. *Catal. Today* **2017**, 286, 78–84.
- (18) Fruchart, D.; Givord, D.; Convert, P.; l'Heritier, P.; Senateur, J. P. The Non-collinear Component in the Magnetic Structure of Mn_4N . J. Phys. F: Met. Phys. 1979, 9, 2431.
- (19) Feng, W. J.; Sun, N. K.; Du, J.; Zhang, Q.; Liu, X. G.; Deng, Y. F.; Zhang, Z. D. Structural Evolution and Magnetic Properties of Mn—N Compounds. *Solid State Commun.* **2008**, *148*, 199–202.
- (20) Kresse, G.; Hafner, J. Ab initio Molecular Dynamics for Open Shell Transitio Metals. *Phys. Rev. B: Condens. Matter Mater. Phys.* **1993**, 48, 13115–13118.
- (21) Kresse, G.; Furthmüller, J. Efficiency of *Ab initio* Total Energy Calculations for Metals and Semiconductors using A Plane-wave Basis Set. *Comput. Mater. Sci.* **1996**, *6*, 15–50.
- (22) Perdew, J. P.; Burke, K.; Ernzerhof, M. Generalized Gradient Approximation Made Simple. *Phys. Rev. Lett.* **1996**, *77*, 3865–3868.
- (23) Blöchl, P. E. Projector Augmented Wave Method. Phys. Rev. B: Condens. Matter Mater. Phys. 1994, SO, 17953–17979.
- (24) Takei, W. J.; Heikes, R. R.; Shirane, G. Magnetic Structure of Mn₄N-Type Compounds. *Phys. Rev.* **1962**, *125*, 1893–1897.
- (25) Monkhorst, H. J.; Pack, J. D. Special Points for Brillouin Zone Integrations. *Phys. Rev. B* **1976**, *13*, 5188–5192.
- (26) Henkelman, G.; Uberuaga, B. P.; Jonsson, H. A Climbing Image Nudged Elastic Band Method for Finding Saddle Points and Minimum Energy Paths. *J. Chem. Phys.* **2000**, *113*, 9901–9904.
- (27) Henkelman, G.; Jónsson, H. A Dimer Method for Finding Saddle Points on High Dimensional Potential Surfaces using Only First Derivatives. *J. Chem. Phys.* **1999**, *111*, 7010–7022.
- (28) Le, T. N.-M.; Liu, B.; Huynh, L. K. SurfKin: An Ab initio Kinetic Code for Modeling Surface Reactions. *J. Comput. Chem.* **2014**, *35*, 1890–1899.
- (29) Shan, N.; Zhou, M.; Hanchett, M. K.; Chen, J.; Liu, B. Practical Principles of Density Functional Theory for Catalytic Reaction Simulations on Metal Surfaces from Theory to Applications. *Mol. Simul.* **2017**, *43*, 861–885.
- (30) Mars, P.; van Krevelen, D. W. Oxidations Carried Out by Means of Vanadium Oxide Catalysts. *Chem. Eng. Sci.* **1954**, *3*, 41–59.
- (31) Fernández, E. M.; Moses, P. G.; Toftelund, A.; Hansen, H. A.; Martínez, J. I.; Abild-Pedersen, F.; Kleis, J.; Hinnemann, B.; Rossmeisl, J.; Bligaard, T.; Nørskov, J. K. Scaling Relationships for Adsorption Energies on Transition Metal Oxide, Sulfide, and Nitride Surfaces. *Angew. Chem., Int. Ed.* **2008**, 47, 4683–4686.
- (32) Abild-Pedersen, F.; Greeley, J.; Studt, F.; Rossmeisl, J.; Munter, T. R.; Moses, P. G.; Skúlason, E.; Bligaard, T.; Nørskov, J. K. Scaling Properties of Adsorption Energies for Hydrogen-containing Molecules on Transition-metal Surfaces. *Phys. Rev. Lett.* **2007**, *99*, 016105.